communications physics

A Nature Portfolio journal

Article

https://doi.org/10.1038/s42005-025-02039-8

Hilbert space fragmentation at the origin of disorder-free localization in the lattice Schwinger model

Jared Jeyaretnam[1,6], **Tanmay Bhore**[1,6], **Jesse J. Osborne**[2], **Jad C. Halimeh**[3,4,5] & **Zlatko Papić**[1]

Lattice gauge theories, the discrete counterparts of continuum gauge theories, provide a rich framework for studying non-equilibrium quantum dynamics. Recent studies suggest disorder-free localization in the lattice Schwinger model, but its origin remains unclear. Using a combination of analytical and numerical methods, we show that Hilbert space fragmentation emerges in the strong coupling limit, constraining particle dynamics and causing sharp jumps in entanglement entropy growth within charge sectors. By analyzing jump statistics, we find that entanglement growth follows a single-logarithmic or weak power-law dependence on time, rather than a double-logarithmic form. This suggests a single ergodicity-breaking regime that mimics many-body localization in finite systems due to fragmentation effects. Our findings clarify the nature of disorder-free localization and its distinction from conventional many-body localization, highlighting how gauge constraints influence thermalization in lattice gauge theories.

Lattice gauge theories (LGTs), originally introduced as powerful approximations to the continuous gauge theories underlying the Standard Model[1–3], have recently generated a flurry of interest for their realizations in synthetic quantum systems[4–7]. Gauge invariance endows LGTs with superselection sectors, determined through Gauss's law by the joint configuration of fermions and gauge fields. In one spatial dimension, it is possible to integrate out the gauge fields, which leaves the matter fields in the presence of an effective local potential furnished by the background charges, i.e., the eigenvalues of the Gauss law generator. The presence of dynamical constraints induced by the Gauss law makes LGTs an attractive platform for exploring various interaction-driven forms of ergodicity breaking, such as many-body localization (MBL)[8–14], Hilbert space fragmentation[15–17], and quantum many-body scars[18–20].

The properties of MBL systems, such as suppressed transport and memory of initial conditions, continue to attract much attention in experiment[21–30]. The onset of MBL has been phenomenologically explained by "local integrals of motion" (LIOMs)[31–33], an extensive set of conserved quasilocal operators whose eigenvalues fully characterize the eigenstates of MBL systems and thereby cause a breakdown of thermalization. The LIOM picture is supported by analytical results for a specific model[34] and numerical simulations of a wider family of MBL models[31,35–49]. Nevertheless, strong finite-size effects often encountered in the numerics[50,51] have recently raised questions about the stability of LIOMs in the thermodynamic limit[52,53].

The standard models of MBL typically involve a static external potential that takes random values and acts as a quenched disorder. By contrast, in LGTs, averaging over superselection sectors assumes the role of an effective disorder average for the matter field. The resulting disorder-free localization[54–76] has been observed by preparing the system in a far-from-equilibrium initial state that is in a superposition of an extensive number of superselection sectors. This makes LGTs reminiscent of other types of translation-invariant lattice models that had been proposed to self-consistently undergo an MBL transition due to interactions or dynamical constraints[77–90].

A salient question is whether the nature of ergodicity breaking in LGTs is indeed of the same kind as in disordered MBL models[35]. For one, the effective disorder in LGTs is discrete due to the integer-valued background charges. Moreover, in a $U(1)$ LGT quenched from the fermonic vacuum state, the growth of entanglement was found to be ultraslow, seemingly following an unusual double-logarithmic dependence on time[56], which was also reported in a disordered Bose-Hubbard chain[91]. Such ultraslow entanglement growth appears distinct from a logarithmic-in-time entanglement growth in conventional MBL systems quenched from product

---

[1]School of Physics and Astronomy, University of Leeds, Leeds, UK. [2]School of Mathematics and Physics, The University of Queensland, St. Lucia, QLD, Australia. [3]Max Planck Institute of Quantum Optics, Garching, Germany. [4]Department of Physics and Arnold Sommerfeld Center for Theoretical Physics (ASC), Ludwig Maximilian University of Munich, Munich, Germany. [5]Munich Center for Quantum Science and Technology (MCQST), Munich, Germany. [6]These authors contributed equally: Jared Jeyaretnam, Tanmay Bhore. e-mail: jared.jeyaretnam@nottingham.ac.uk

states[92–94]. While the latter is a natural consequence of the LIOM-induced dephasing processes[31], to the best of our knowledge there has been no understanding yet of the putative double-logarithmic growth of entanglement in a $U(1)$ LGT.

In this paper, we study ergodicity breaking in a $U(1)$ LGT – the one-dimensional (1D) Schwinger model – using a combination of analytical and numerical tools, including degenerate perturbation theory, exact diagonalization, and matrix-product states. We characterize the model using both spectral and eigenstate properties, focusing on entanglement in particular, and we contrast the results against conventional MBL in disordered spin chains. We find that the strong-coupling limit of the theory is dominated by an approximate Hilbert space fragmentation[95], which strongly impacts the properties of finite-size systems, causing visible deviations of the level statistics from standard random-matrix-theory ensembles. We identify the mechanism of entanglement growth as sharp jumps between the weakly-connected Krylov sectors of the Hilbert space for a given charge sector of the gauge field. The averaging over sectors reproduces the slow growth of entanglement previously observed[56]; however, a closer look at the statistics of jump times suggests that the growth can be more simply explained as a weak power law or (single) logarithmic dependence on time. Our results point to the existence of a single ergodicity-breaking regime in the lattice Schwinger model, which originates from Hilbert space fragmentation but mimics conventional MBL in numerically-accessible system sizes.

Results

The dynamical phase diagram of the lattice Schwinger model

The Schwinger model describes quantum electrodynamics on a one-dimensional (1D) lattice[96]. In the Wilson formulation[1], the model describes the coupling between matter fields that reside on lattice sites and $U(1)$ gauge fields that reside on the links between the sites, see Fig. 1(a). The model is described by the Kogut-Susskind Hamiltonian[2]

$$\hat{H}_{\mathrm{Sch}} = -iw\sum_{n=1}^{N-1}\left[\hat{\Psi}_n^{\dagger}\hat{U}_n\hat{\Psi}_{n+1} - \mathrm{H.c.}\right] + J\sum_{n=1}^{N-1}\left(\hat{L}_n + \frac{\theta}{2\pi}\right)^2 + m\sum_{n=1}^{N}(-1)^n\hat{\Psi}_n^{\dagger}\hat{\Psi}_n\,, \tag{1}$$

where $\hat{\Psi}_n, \hat{\Psi}_n^{\dagger}$ are the fermionic annihilation and creation operators on the nth lattice site, while $\hat{U}_n = e^{i\hat{\phi}_n}$ are the $U(1)$ parallel transporters defined on the bond between sites n and $n+1$, see Fig. 1(a). Each $\hat{U}_n$ has a corresponding electric field operator $\hat{L}_n = -i\partial/\partial\phi_n$, such that the commutation relation $[\hat{L}_n, \hat{U}_n] = \hat{U}_n$ holds. θ describes a constant classical background field and can be used to tune between the confined ($|\theta| < \pi$), and deconfined ($|\theta| = \pi$) phases. Throughout this paper, we will assume open boundary conditions (OBCs). A self-contained derivation of the LGT model (1) from the continuum theory is provided in Supplementary Note 1.

Physical states of the lattice gauge theory are constrained by Gauss' law, which is encoded as a set of local constraints on the lattice. Specifically, to ensure gauge invariance, we consider the generators of the Gauss law,

$$\hat{G}_n = \hat{L}_n - \hat{L}_{n-1} - \Psi_n^{\dagger}\Psi_n + \frac{1}{2}[1-(-1)^n]\,, \tag{2}$$

such that $[\hat{H}_{\mathrm{Sch}}, \hat{G}_n] = 0$. Physical states are defined as the eigenstates of $\hat{G}_n$, i.e., $\hat{G}_n|\Psi_{\{q_\alpha\}}\rangle = q_n|\Psi_{\{q_\alpha\}}\rangle$, where the eigenvalues $\{q_\alpha\}$ and corresponding states $|\Psi_{\{q_\alpha\}}\rangle$ define the background charge sector of the Hilbert space.

After a Jordan-Wigner transformation (see Supplementary Note 2), Gauss' law allows us to sequentially integrate out the gauge fields, resulting in an effective spin-1/2 Hamiltonian [see Fig. 1(a)]:

$$\hat{H}_{\{q_\alpha\}} = \hat{H}_{\pm} + \hat{H}_{ZZ} + \hat{H}_q, \tag{3}$$

which explicitly depends on the background charge sector $\{q_\alpha\}$. The three terms are given by

$$\hat{H}_{\pm} = w\sum_{j=1}^{N-1}\left[\hat{\sigma}_j^{+}\hat{\sigma}_{j+1}^{-} + \mathrm{H.c.}\right], \tag{4}$$

$$\hat{H}_{ZZ} = \frac{J}{2}\sum_{j=1}^{N-2}\sum_{k=j+1}^{N-1}(N-k)\hat{\sigma}_j^z\hat{\sigma}_k^z\,, \tag{5}$$

$$\hat{H}_q = \sum_{k=1}^{N}\left(h_k + \frac{m}{2}(-1)^k\right)\hat{\sigma}_k^z\,, \tag{6}$$

$$h_k = \frac{J}{2}\left((N-k)\frac{\theta}{\pi} - \left\lceil\frac{N-k}{2}\right\rceil + 2\sum_{j=k}^{N-1}\sum_{i=1}^{j}q_i\right), \tag{7}$$

where $\hat{\sigma}^{\pm} \equiv (\hat{\sigma}^x \pm i\hat{\sigma}^y)/2$ denote the standard Pauli raising and lowering operators, and $\lceil\cdots\rceil$ is the ceiling function. The three terms in the Hamiltonian correspond, respectively, to the number-conserving hopping of fermions across the bonds (the XY spin term), the interactions, and the effective local field generated by the background charges $\{q_\alpha\}$. Note the asymmetric nature of long-ranged couplings in $\hat{H}_{ZZ}$: each spin interacts with all spins to its left with a constant strength, while the strength of interaction decreases linearly with distance for all spins to its right. The Hamiltonian has a $U(1)$ magnetization-conservation symmetry, equivalent to charge conservation in the fermionic LGT, and here onward we restrict

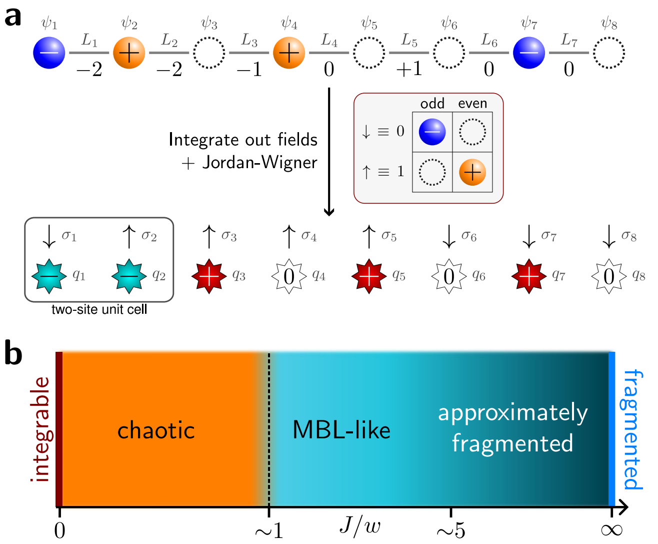

Fig. 1 | Overview of this work. a The 1D lattice Schwinger model (top) describes quantum electrodynamics on a lattice. Fermionic degrees of freedom ψ_n on odd (even) sites represent the presence or absence of an electron (positron), while the electric fields L_n reside on the bonds and mediate coupling between the particles. In 1D, one can integrate out the fields and apply a Jordan-Wigner transform, which results in an XY-type model for spins $\sigma = \uparrow, \downarrow$. The dynamical fields are replaced by static background charges q_n, which act as a disorder potential for spins. **b** Schematic phase diagram for the 1D lattice Schwinger model as a function of the dimensionless coupling ratio J/w [see Eq. (3) for details]. In the weak-coupling limit $J/w \to 0$, the model reduces to an integrable XY spin chain. In the thermodynamic limit, any finite J breaks integrability, resulting in a chaotic phase. Around $J/w \sim 1$, an ergodicity-breaking transition, consistent with an onset of MBL (many-body localization), has previously been observed[56]. However, the nature and extent of the MBL phase is difficult to ascertain in finite-size systems due to its proximity to the regime dominated by Hilbert space fragmentation. The latter is exact at $J/w \to \infty$ and, as shown in this paper, strongly affects the properties of numerically-accessible systems even at $J/w \sim 5$.

the Hamiltonian to the largest symmetry sector with zero total magnetization (i.e. zero charge). For simplicity, we focus on the massless case, $m = 0$, and we express the hopping amplitude w and interaction strength J in units $\hbar = 1$; however, we expect the phenomenology to be broadly similar for any $m \ll J$. We also normalize the Hamiltonian by picking $w = 1$. Finally, we choose $\theta = \pi$, placing the model in the deconfined phase, in order to rule out confinement as an explanation for the observed phenomena.

The full state of the system encodes the degrees of freedom of both fermions and gauge fields: it is spanned by tensor products, $|\Psi\rangle_0 = |\Psi\rangle_f \otimes |\Psi\rangle_g$, where $|\Psi\rangle_{f/g}$ is the state of the fermions/gauge fields. For the fermions, we focus on the vacuum state or the Néel state of fermions, $|\Psi\rangle_f = |101010\ldots\rangle \equiv |\mathrm{vac}\rangle_f$, while other choices of fermionic states are discussed in Supplementary Note 3. For $|\Psi\rangle_g$, following Brenes et al.[56], we consider a uniform superposition of three eigenstates of the electric field operators – see Methods. Due to the constraint between the gauge fields $\hat{L}_n$ and the background charges q_n, our initial state therefore effectively encodes a superposition over the charge sectors.

The presence of disconnected charge sectors in the model, each evolving independently in time, produces an effective disorder landscape: each charge sector acts as a disorder realization, whose distribution is set by the full initial state of the fermions and gauge fields. This gives rise to a dynamical phase diagram sketched in Fig. 1(b). At $J/w = 0$, the model reduces to an integrable XY spin chain. Finite values of $J/w \lesssim 1$ make the dynamics chaotic. Increasing the coupling further to $J/w \gtrsim 1$ breaks ergodicity and was previously suggested to give rise to disorder-free localization[56,97]. Treating the gauge field as a spin-1/2 degree of freedom, similar dynamics were found after including the four-fermion interaction term[74]. On the other hand, the entanglement entropy growth at $J/w = 10$[56] suggested a much slower and parametrically different growth compared to the conventional LIOM picture of MBL, raising the possibility of a distinct MBL-like regime in the strong-coupling limit of the Schwinger model. Below we provide a detailed characterization of the phase diagram in Fig. 1(b), focusing on the strong-coupling regime.

Level statistics and the density of states

A standard metric of quantum chaos is the level spacing ratio[98], $r = \min\{s_n, s_{n+1}\}/\max\{s_n, s_{n+1}\}$, which characterizes the spacing of adjacent energy levels $s_n = E_{n+1} - E_n$. After all symmetries are resolved, the averaged energy gaps of an integrable or MBL system are expected to follow the Poisson distribution with the average ratio $\langle r\rangle_P \approx 0.386$, while those of chaotic systems with time-reversal symmetry obey the Gaussian Orthogonal Ensemble with $\langle r\rangle_{\mathrm{GOE}} \approx 0.536$[99]. We note that the spin Hamiltonian in (3) is real in the computational basis and thus time-reversal symmetric, hence its ergodic phase should belong to the GOE class.

In Fig. 2(a), we calculate the sector-averaged level spacing ratio $[\langle r\rangle]_q$ as a function of the coupling strength J. We consider system sizes up to $N = 18$ and 1000 randomly chosen background charge sectors. Here, $[\ldots]_q$ indicates an average overcharge sectors, while an average over eigenstates is specified by $\langle\ldots\rangle$. For $N \le 16$, we calculate the full spectrum and truncate to the k states closest to the peak in the density of states (DOS), with k the smaller of 500 or one-third of the Hilbert space dimension. For $N = 18$, we use the shift-invert algorithm[100] to obtain 500 eigenvalues closest to a target energy: we choose this target to be the modal classical energy (diagonal matrix element of the Hamiltonian), which is taken as an approximation to the DOS peak.

To understand Fig. 2(a), we first note that the model is integrable for $J = 0$[101], with the average level spacing ratio equal to the Poisson value. Upon introducing a non-zero but small J, integrability is broken, and we observe that $[\langle r\rangle]_q$ increases away from the Poisson value, steadily approaching the GOE value for a broad range of coupling strengths below $J \approx 0.1$. This is observed for all but the smallest system sizes (N = 8, 10), suggesting that finite-size effects in our model are considerably stronger than in disordered MBL models[35]. In the regime $J \lesssim 0.1$, we expect the system to obey the Eigenstate Thermalization Hypothesis (ETH), with various consequences for the dynamics, such as relaxation of local observables to their thermal values, which were observed by Brenes et al.[56] for $J/w = 0.1$.

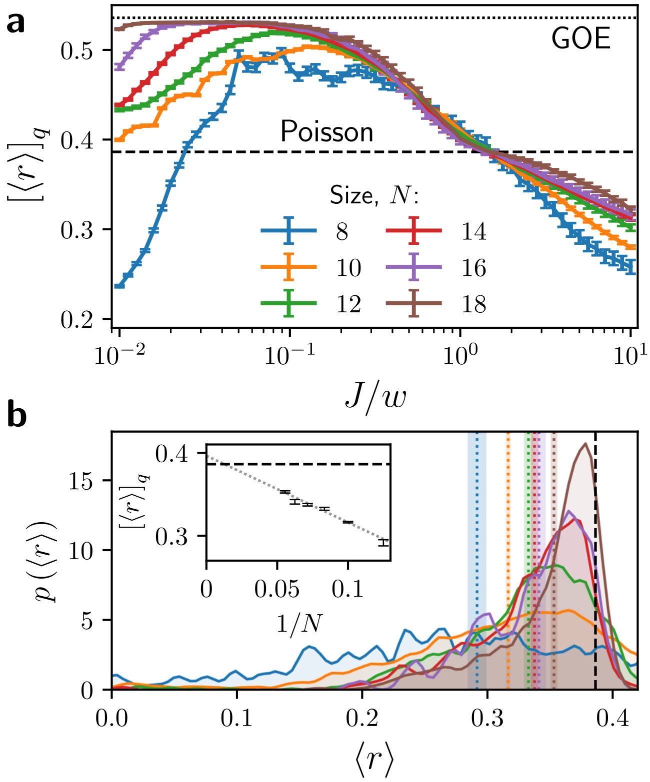

Fig. 2 | Level statistics of the model. a $\{q_\alpha\}$-averaged level spacing ratio as a function of the coupling strength parameter J/w. We truncate each spectrum to the $k = \min(1000, \mathcal{N}/3)$ states with energies closest to the peak in the density of states, or an approximation thereof for system size $N = 18$, where $\mathcal{N}$ is the Hilbert space dimension. We also show the Poisson and Gaussian Orthogonal Ensemble (GOE) values as dashed and dotted black lines, respectively. The narrow localization-like plateau appears at around $J/w \sim 1.5$. **b** Distribution of the level spacing ratio across different charge sectors for fixed $J/w = 5$. The average values are also shown as vertical dotted lines (with uncertainties shown by the shaded regions), and the black dashed line indicates the Poisson value. While the distributions clearly shift towards Poisson as N increases, there is considerable weight at sub-Poisson values. The inset shows the trend in the $\{q_\alpha\}$-averaged value with $1/N$, showing that it likely reaches Poisson in the thermodynamic limit. [We use all charge sectors for N = 8, 10, 1000 for N = 12, 14, 18, and 250 for N = 16. Uncertainties in all panels are calculated as the standard uncertainty in the mean.].

Upon increasing J/w beyond 0.2, we see a deviation from GOE statistics with $[\langle r\rangle]_q$ steadily decreasing until a plateau forms at the Poisson value at around $J/w = 1.5$. This transition from GOE to Poisson statistics marks the onset of an MBL-like regime at intermediate coupling strengths. However, upon further increasing J/w, we observe a further decrease of $[\langle r\rangle]_q$, even dropping below the Poisson value for all system sizes considered. This indicates the level statistics of the system is no longer well described by one of the standard random-matrix theory ensembles. Such a dip is caused by the presence of a large number of (near)-degeneracies in the spectrum, the expected source of which could be an unresolved or an emergent symmetry. However, we note that model hosts no such extra symmetry, even within the zero-magnetization sector. In Fig. 2b, we show the distribution of $\langle r\rangle$ – that is, the average level spacing ratio within individual charge sectors – across different charge sectors, for various system sizes at $J/w = 5$. The distribution becomes more sharply peaked and moves towards the Poisson value with increasing system size; plotting the sector average against $1/N$, as in the inset, shows that it is likely the level spacing ratio will attain the Poisson value in the thermodynamic limit $N \to \infty$.

To understand the anomalous features in the level statistics, in Fig. 3 we plot the density of states (DOS) for three selected values of J in a single charge sector at $N = 16$. We also show the averaged DOS across 250 charge sectors.

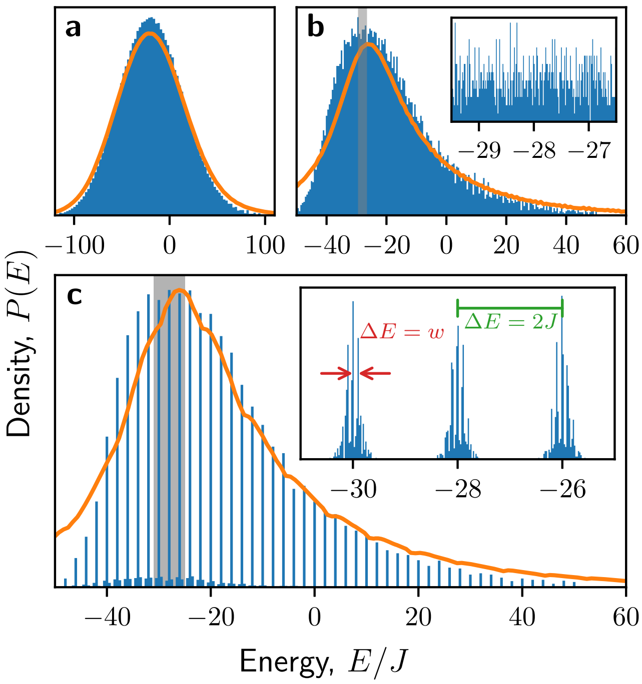

Fig. 3 | Density of states (DOS) for a single charge sector. We show the sector $q_\alpha = \left[1\,\bar{1}\,0\,0\,1\,\bar{1}\,1\,0\,0\,1\,0\,0\,0\,\bar{1}\,\bar{1}\,0\,0\,0\right]$, where $\bar{1} \equiv -1$, and use coupling strengths (**a**) $J = 0.1$, (**b**) $J = 1$, and (**c**) $J = 5$. All data is for system size $N = 16$ and $w = 1$. We also show, in orange, the averaged DOS across 250 superselection sectors. For (**b**) and (**c**), the insets show a close-up around the DOS peak, with the zoom region indicated by gray shading in the main panels; while the overall DOS looks similar for $J = 1$ and $J = 5$, we see that for $J = 5$ the spectrum has split into well-separated "towers" separated by intervals of $2J$. These towers are themselves split into peaks with intervals of w.

Furthermore, we choose to normalize the spectrum by dividing by J. For small $J = 0.1$, in Fig. 3a, we find that the spectrum is relatively symmetric, with a peak close to $E = 0$ and a smooth Gaussian form consistent with typical chaotic systems. However, for increasing J, the spectrum gains a large positive tail, while both the peak and the mean energy shifts towards the negative. This skew is explained by the $\hat{H}_{ZZ}$ term in Eq. (3): this is long-ranged, antiferromagnetic, and features a double-sum over terms with $\mathcal{O}(N)$-size coefficients, and therefore can give a large positive contribution up to $\mathcal{O}(JN^3)$ for certain states with many aligned spins. On the other hand, the long-ranged antiferromagnetism leads to large frustration in trying to find the ground state, and empirically this will have an energy of $-\mathcal{O}(JN^2)$.

The dips in the level spacing ratio $\langle r \rangle$ are expected to be accompanied by sharp peaks in the DOS as energies cluster together to become almost degenerate. Upon increasing the value of J, this is indeed what we observe as the DOS becomes increasingly stratified, with sharp peaks clearly visible at $J/w = 5$ in Fig. 3(c). These sharp peaks are almost equally spaced in energy with a separation of $2J$. However, the slices used for calculating $\langle r \rangle$ in Fig. 2 should fit entirely within a single peak for the largest system sizes considered, and so this alone cannot explain the dip in $\langle r \rangle$ below $\langle r \rangle_{\mathrm{GOE}}$. Further zooming in on these peaks, we can see that they are themselves jagged and irregular, with principal peaks at intervals of w. Therefore, not only are the strong-coupling terms $\hat{H}_{ZZ}$ and $\hat{H}_q$ restricting basis states with different classical energies from mixing effectively, these classical energy levels are also not being well-mixed by the hopping term $\hat{H}_\pm$. This indicates that there is a dynamical restriction or Hilbert space fragmentation present in the model, which will be explored in detail below.

Hilbert space fragmentation at strong coupling

In the limit $J/w \to \infty$, the Hamiltonian (3) becomes diagonal and its eigenstates are simply product states in the z-basis. We would like to understand the spectrum of the model as we reintroduce a perturbatively small w. With $m = 0$, the coefficients in both $\hat{H}_{ZZ}$ and $\hat{H}_q$ take values which are multiples of $J/2$, while the constituent Pauli operators can only take the values ± 1, thus it is clear that with $w = m = 0$, energies will take discrete values separated by (at least) J. In fact, the separation is always at least $2J$ (see Supplementary Note 4). The width of the spectrum will then be $\mathcal{O}(JN^3)$ (dominated by $\hat{H}_{ZZ}$), which implies there are at most $\mathcal{O}(N^3)$ of these energy levels. With 2^N states in the Hilbert space, the eigenenergies will be massively degenerate in the thermodynamic limit. We label these degenerate towers $\{\mathcal{K}_a\}$, $a \in \mathbb{Z}$.

As we perturbatively reintroduce w, we expect naively that the degenerate towers will broaden to a width $\mathcal{O}(Nw)$ due to $\hat{H}_\pm$. However, we instead find that the structure of these towers, and the interplay between $\hat{H}_{ZZ}$ and $\hat{H}_q$, imposes a kinetic constraint that fractures the towers into disconnected subspaces. It can be shown (see Supplementary Note 4) that it costs zero energy to exchange two spins at sites ℓ and $\ell + 1$, $|01\rangle \leftrightarrow |10\rangle$, only if

$$\sum_{j=1}^{\ell-1} \hat{\sigma}_j^z + 2\sum_{j=1}^{\ell} q_j = (\ell \bmod 2) - \frac{\theta}{\pi}\,, \tag{8}$$

while any other dynamics within a tower must occur as a second-order off-shell process involving another tower and is therefore suppressed by a factor of at least $\mathcal{O}(w/J)$.

The background charges therefore set the condition for resonant hopping to occur. For the initial state $|\,\mathrm{vac}\,\rangle$, twice the sum of the background charges is $\hat{L}_\ell(0)$, and so the initial electric field between two sites directly controls this hopping. Physically, we can interpret this as the manifestation of the 1D Coulomb law.

More generally, $\sum_{j=1}^{\ell-1} \hat{\sigma}_j^z - (\ell \bmod 2)$ counts the fermionic charge (that is, in terms of electrons e^- and positrons e^+) to the left of the candidate spins, as shown in Fig. 4a. Since we have number conservation and half-filling, which is equivalent to enforcing charge neutrality, this quantity is equal and opposite on the other side of the bond. Figure 4b then illustrates how exchange of spins results in the creation or annihilation of an $e^- e^+$ pair, increasing or decreasing L_ℓ by one. If Eq. (8) is satisfied, then with $\theta = \pi$ this will take $L_\ell + \theta/2\pi$ from $-1/2$ to $+1/2$ (or vice versa), such that the energy of the electric field $\propto (L_\ell + \theta/2\pi)^2$ is unchanged. The net effect is that starting from a particular initial state, only certain parts of the chain – "active regions" – will permit dynamics in the large-J limit [Fig. 4c]. We therefore see that each degenerate energy level $\mathcal{K}_a$ fractures into a set of subspaces $\{\mathcal{K}_a^b\}$ which are disconnected under the action of $\hat{H}_\pm$ [Fig. 4d]. Each of these subspaces is a Krylov subspace[19], i.e., a space obtained by repeatedly applying an operator $\hat{O}$ to an initial state $|\psi\rangle$, where, in this case, $|\psi\rangle$ is a $\hat{\sigma}^z$-basis state and $\hat{O}$ is the projection of $\hat{H}_\pm$ into a degenerate tower $\mathcal{K}_a$.

The fragmentation partially explains the behavior seen in the level statistics at large J in Fig. 2(a). Because the resonance condition (8) is invariant under rearrangements of spins that do not cross the bond under consideration, the active regions will have fully independent dynamics in the large-J limit. We can therefore typically decompose each Krylov subspace and its effective Hamiltonian (given by the projection of $H_\pm$),$\mathcal{K} = \mathbb{C}^{n_1} \otimes \mathbb{C}^{n_2} \otimes \mathbb{C}^{n_3} \otimes \ldots$ and $\hat{H}_{\mathcal{K}} = \hat{H}_1 + \hat{H}_2 + \hat{H}_3 + \ldots$, where the n_i is the total Hilbert space dimension of the ith active region, and $\hat{H}_i$ is the part of $\hat{H}_\pm$ acting only on $\mathbb{C}^{n_i}$. The eigenvalues of $\hat{H}_{\mathcal{K}}$ will therefore be sums of individual eigenvalues, $E_{\mathcal{K}} = \varepsilon_1 + \varepsilon_2 + \varepsilon_3 + \ldots$. In general, the active regions and therefore the n_i will be small, such that the ε_i will be simple algebraic numbers (often integers, even zeros), leading to many accidental degeneracies in E and thus bringing $\langle r \rangle$ below the Poisson value. This also explains the spacing by w observed in Fig. 3c.

As $N \gg 1$, the active regions will typically remain small, but increase in number, such that the distribution of eigenvalues $\sum_j \varepsilon_j$ would begin to resemble something closer to a Poisson distribution. The width of this distribution would also grow as $\mathcal{O}(\sqrt{N})$, weakening the strong separation in energy scales and therefore increasing mixing between states belonging to

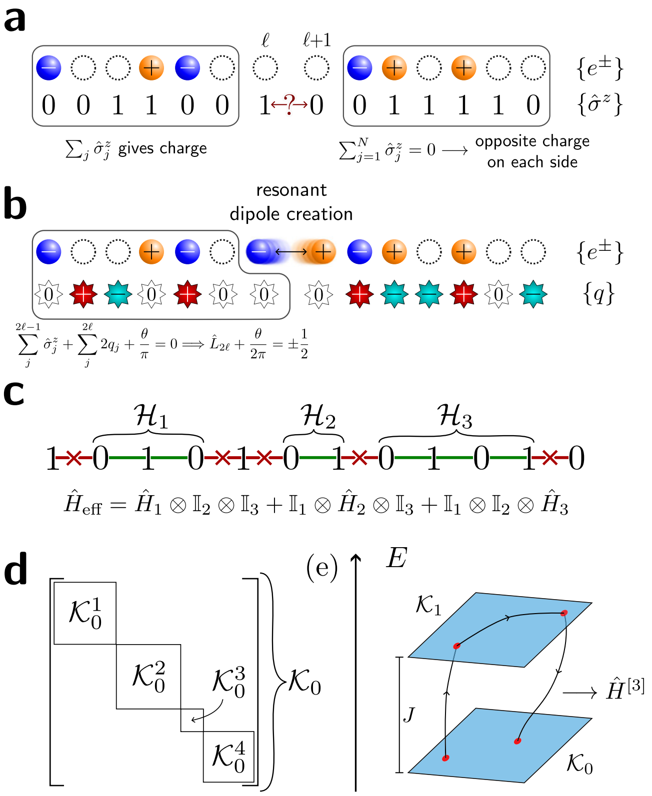

Fig. 4 | Energy levels of the model are fragmented by the resonance condition Eq. (8). **a** The parity $\sum_j \hat{\sigma}_j^z$ over some regions gives the total charge in the original gauge theory; this must sum to zero over the whole chain. **b** Exchanging $|10\rangle \leftrightarrow |01\rangle$ at sites 2ℓ and $2\ell+1$ creates an e^-e^+ pair. This is resonant if the combination of gauge and background fields $L_{2\ell} + \theta/2\pi = \pm 1/2$ both before and after this process. **c** For a particular charge sector and spin configuration, only certain bonds satisfy the previous condition and thus permit dynamics in the large-J limit. These "active regions" are independent and so the effective Hamiltonian is a sum of local commuting terms. **d** Each energy level $\mathcal{K}_a$ therefore fragments into Krylov subspaces $\{\mathcal{K}_a^b\}$ which are disconnected under the action of $\hat{H}_{\pm}$. **e** For finite J, degenerate perturbation theory (see Methods) allows us to obtain an effective Hamiltonian within $\mathcal{K}_0$ as an expansion in powers of w/J. For example, a series of three spin exchanges via a nearby energy level contributes a term to the third-order effective Hamiltonian $H^{[3]}$ of magnitude $\mathcal{O}(w^3/J^2)$.

each tower. Figure 2b indeed shows that that the distribution of the level spacing ratio tends towards the Poisson value as we keep J/w fixed and increase N.

While the Hilbert space fragmentation discussed above is only strictly valid for $J/w \to \infty$, the structure and dynamics of the model for large but finite J/w can be captured using degenerate perturbation theory (DPT), by which the effective Hamiltonian within a J-tower $\mathcal{K}_0$ is expanded in orders of w/J, $\hat{H}_{\text{eff}} = \hat{H}^{[0]} + \hat{H}^{[1]} + \hat{H}^{[2]} + \ldots$, with $\hat{H}^{[n]} = \mathcal{O}(w^n/J^{n-1})$, see Methods. This means that evolution under the Hamiltonian up to nth order, which we label DPT(n), will typically capture the dynamics up to $wt = \mathcal{O}((J/w)^{n-1})$, so long as $J/w \gg 1$, and will involve processes with n virtual hops via $n-1$ (not necessarily unique) energy levels. An illustration of a third-order process is given in Fig. 4e. In the Methods, we demonstrate that third-order DPT accurately captures the dynamics of local observables and entanglement growth during intermediate times $wt \lesssim 10^3$. However, to capture the putative double-logarithmic entanglement growth regime, discussed next, one would have to extend DPT to much higher orders, which was not practically feasible.

Late-time entanglement growth

Entanglement provides a powerful diagnostic of thermalization and its breakdown. We characterize the entanglement of a pure state $|\psi\rangle$ via its entanglement entropy S_E for a bipartition of the system into subsystems A and B:

$$S_E = -\text{tr}(\rho_A \ln \rho_A), \quad \rho_A = \text{tr}_B \rho\,, \tag{9}$$

where tr_B is the trace over degrees of freedom in B, and $\rho = |\psi\rangle\langle\psi|$ is the density matrix for the full system. In chaotic systems evolving under unitary dynamics, S_E increases as a power-law in time, $S_E(t) \sim t^{\gamma}$[102]. By contrast, in MBL systems the growth is logarithmic, $S_E(t) \sim \ln t$[92–94]. Previous numerical simulations[56] of the model in Eq. (3) argued for an even slower growth of entanglement entropy in the strong-coupling regime, conjecturing that it follows an unusual double-logarithmic dependence $S_E(t) \sim \ln(\ln t)$ at late times. Here we explore the origin of such slow growth and its relation to Hilbert space fragmentation, focusing on individual charge sectors.

For short times $wt < J$ we expect the dynamics to remain entirely within the initial subspace $\mathcal{K}_0^0$, while at later times, higher-order processes allow the dynamics to escape both this subspace and the containing energy level. However, we find that the proportion of the state which lies outside of the initial subspace saturates by the time the proposed sub-logarithmic entanglement growth sets in. We see a similar trend in quantities that measure the distribution of coefficients across the computational ($\hat{\sigma}^z$) basis, such as the inverse participation ratio[31]. This implies that the ultraslow growth in entanglement following the initial transient is driven not by changes to the distribution of coefficients across the basis, but due to correlations built up between configurations of particles on either side of the bipartition. From the numerical data, we also observe that $S_E(t)$ displays very different behaviors in individual charge sectors: while it quickly increases in some sectors, in others it remains close to zero for the entire accessible range.

In a particle-number conserving system, the reduced density matrix ρ_A, Eq. (9), can be block-diagonalized, $\rho_A = \bigoplus_n p(n)\rho_A(n)$ with $\text{tr}\rho_A(n) = 1$, where $\rho_A(n)$ corresponds to those states with n particles in subsystem A, such that $p(n)$ is the probability distribution of particle number in A. This allows us to decompose the total entropy into two contributions[27,103]: the number entropy S_N, which represents uncertainty in particle count, and the configurational entropy S_C, which expresses our uncertainty in how those fixed numbers of particles are arranged:

$$S_E = S_N + S_C\,, \tag{10}$$

$$S_N = -\sum_n p(n) \ln p(n)\,, \tag{11}$$

$$S_C = -\sum\nolimits_n p(n)\text{tr}[\rho_A(n) \ln \rho_A(n)]\,. \tag{12}$$

Below we will argue that the origin of the ultraslow growth of entanglement is discrete jumps in the configurational entropy S_C, which occur in particular charge sectors at well-defined times, and it is only after averaging over charge sectors that a smooth growth in the entropy emerges. On the other hand, the number entropy S_N saturates at relatively short times and so does not play a role in this slow growth.

These jumps correspond to the resolution of near-degeneracies that originate from the fractured nature of the Hilbert space. In the large-J limit, the unperturbed basis states are massively degenerate. Each successive order n of degenerate perturbation theory, which describes the system away from the limit, then provides a correction $\mathcal{O}(w^n/J^{n-1})$ to the energies, splitting these degeneracies. The dynamics will resolve these corrections at a time $wt \approx (2J/w)^{n-1}$, resulting in a jump in the entanglement entropies as the corresponding states hybridize[104]

In Fig. 5a–c we show the entanglement, number, and configurational entropies, respectively, for the Schwinger model with $J = 8$, including both the results from each of 512 individual charge sectors as well as the mean and median over sectors. Here, the median is defined as the median value at each moment in time – it is important to note that, as a complete trajectory, this does not necessarily represent a single "typical" charge sector. Throughout this section, we also convolve individual charge sectors with a narrow

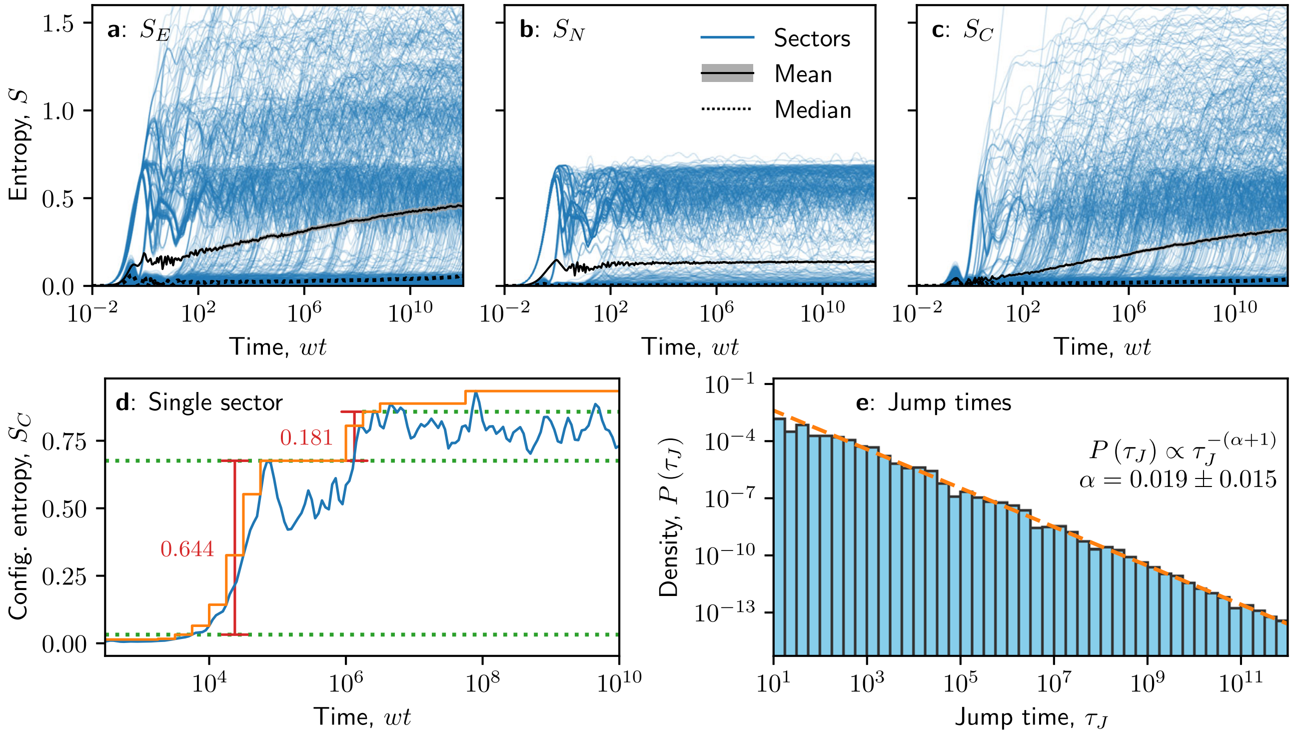

Fig. 5 | Jumps in entanglement following a quench from the vacuum state. **a–c** Entanglement entropy S_E, number entropy S_N, and configurational entropy S_C, respectively [Eqs. (10)-(12)], for coupling strength $J = 5$ and system size $N = 16$. In each figure, we show the individual results for each of 1000 charge sectors (blue), as well as the mean (black solid) and median (black dotted) averages over sectors. The standard error in the mean is shaded in gray. Jumps in the configurational entropy are clearly visible across a wide range of time scales, spanning many orders of magnitude, with a single exemplary charge sector shown in (**d**). By taking the cumulative maximum $\sup_{\tau<t_j} S(\tau)$ of the entropy growth at discrete times t_j, thus approximating it as a series of steps (orange), we can calculate the heights and times τ_J of the jumps (red). **e** Histogram of jump times $\{\tau_J\}$, weighted by jump height. A clear fit to a power law (orange dashed line) is observed, with $P(\tau_J) \propto \tau_J^{-(\alpha+1)}$ and $\alpha = 0.019 \pm 0.015$.

Gaussian window to eliminate high-frequency oscillations; this is not necessary for the mean and median.

There are a few noteworthy features in Fig. 5(a)–(c). The most prominent is the very large spread in the entropies of different charge sectors: some of these stay close to zero, while some attain values two or three times larger than the mean. This is especially true for the number entropy, S_N, which saturates quickly to a small value, with only certain charge sectors attaining values that cluster around $\sim \ln(2)$, which indicates the spread of a single particle across the boundary. Furthermore, for the configurational entropy S_C, we observe that growth in individual charge sectors occurs via prominent jumps from one plateau to another (up to some weaker fluctuations around these plateaus). The initial jumps from near-zero to values around $S_C \approx 0.5$ are visible from $t = 10^1$ all the way up to the latest times accessible, $t = 10^{12}$. We also observe that the median lags well behind the mean, staying close to zero at all numerically accessible times. Taken together, these features tell us that the slow growth in the entanglement entropy S_E is driven not by steady growth across charge sectors, but by rapid jumps in the configurational entropy of individual sectors. It is only when we average over the sectors that these jumps are smoothed out into the slow "double-logarithmic" growth found by Brenes et al.[56].

We are therefore interested in characterizing the jumps in configurational entropy, as these could offer deeper insight into the functional form of the entanglement growth. Figure 5d shows the illustrative behavior of $S_C(t)$ for a single charge sector. By taking a cumulative maximum of $S_C(t)$ in a particular charge sector, i.e., $\sup_{\tau<t_j} S_C(\tau)$, at discrete time intervals t_j, we are able to locate intervals of growth in $S_C(t)$, followed by plateaus during which it does not exceed its historic maximum[104]. Specifically, using intervals of $\Delta\log_{10}(t) = 0.25$, we consider periods where the cumulative maximum increases by at least 0.05 in each consecutive interval. We identify these periods as the jumps, calculating their height ΔS_C as the difference in $\sup_{\tau<t_j} S(\tau)$ between the beginning and end, and the jump time τ_J as the geometric midpoint of the start and end times.

Finally, in Fig. 5e, we show the distribution of jump times τ_J, where we have weighted the contribution of each jump to the histogram by the corresponding jump height ΔS_C. Once this distribution is computed, we fit it to a power law in time, $P(\tau_J) \propto \tau_J^{-(\alpha+1)}$. We note that, across various values of N and J, the value of this exponent is not sensitive to the exact parameters used in the jump-finding algorithm, or even to the use of the jump heights as weightings, relative to the calculated errors.

The intuition here is that, if the entropy growth is driven by jumps at late times, then the integral of jump distribution will give back the configurational entropy, i.e., if $P(\tau_J) \propto \tau_J^{-(\alpha+1)}$, then $S_C(t) = S_\infty - S_0 t^{-\alpha}$, with a power-law decay towards a steady-state saturation value S_∞. We confirm this intuition in Fig. 6. Firstly, in Fig. 6a, we show the sector-averaged S_C for $J = 8$ and several system sizes, all showing power-law decay towards a steady-state value, in agreement with the ansatz. Furthermore, in the inset of Fig. 6a, we show the difference between S_C and S_∞ on a log-log scale, verifying that these are indeed power-law decays.

We repeated the procedure above for a spread of different N and J, calculating α both by characterizing the jump times and by fitting S_C to a power law. In Fig. 6b, for $J = 8$, we show α as a function of N, while in Fig. 6c, we plot α against J for fixed $N = 16$. These show a clear trend towards $\alpha = 0$ for increasing N and J, which would be consistent with logarithmic growth $S(t) \sim \ln(t)$. We further see a trend of increasing saturation time for $S(t)$, which is evidence of unbounded entanglement growth in the thermodynamic limit. Taken together this suggests that, within the times accessible to double-precision numerics, the available data for entanglement growth at

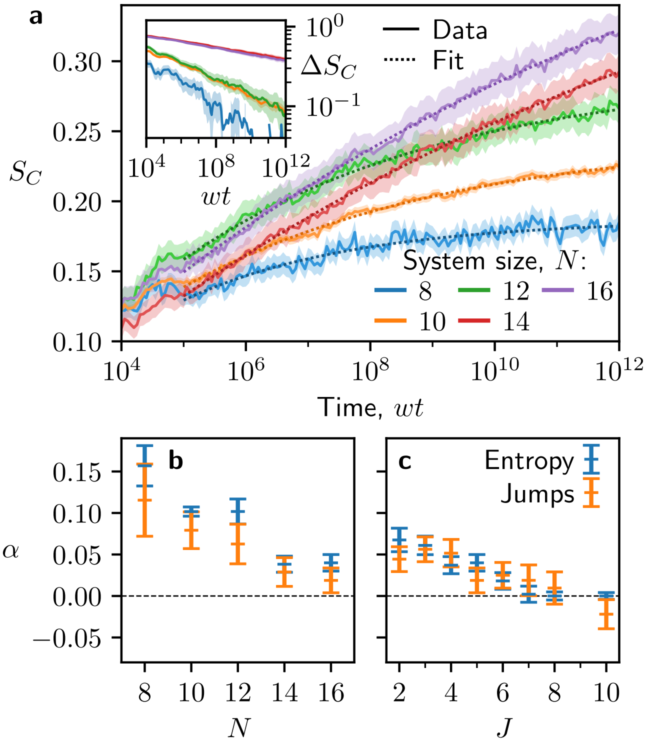

Fig. 6 | Jump time analysis. a Sector-averaged configurational entropy, $S_C(t)$, for coupling strength $J = 5$ and system sizes $N = 8$--16 (solid lines). For each N we fit a power-law of the form $S_C(t) = S_\infty - S_0 t^{-\alpha}$ (dotted lines). In the inset, we show the power-law decay towards the fitted saturation value, $\Delta S_C = S_\infty - S_C(t)$ for each N. The shaded area indicates the standard uncertainty in the mean. **b** The fitted exponent α as a function of N, calculated both from the entropy [as per panel (a)] (blue), or from the jump times [as per Fig. 5(e)] (orange), for $J = 5$. **c** The same as (**b**), but plotting the power-law exponent as a function of J for fixed $N = 16$. We see good agreement between both methods of extracting α. [We use all charge sectors for $N \leq 10$, and otherwise 1000. Uncertainties in (**b**) and (**c**) are given by twice the standard uncertainty in the fit.].

$J/w \gg 1$ is consistent with a single logarithm and it is not necessary to invoke double-logarithmic scaling.

We note that our analysis above bears similarity with the one for the disordered XXZ model studied by Ghosh et al.[104]. However, the latter model shows jumps in the number entropy, which were used to model the double-logarithmic growth of particle fluctuations in the MBL phase. In our case, the particle fluctuations appear strongly suppressed at all accessible time-scales, and it is the configurational entropy that undergoes jumps which give rise to the slow growth of entanglement. We present a more detailed comparison between the $U(1)$ LGT and disordered XXZ models in Supplementary Note 5. In the SI, we also study a variant of the XXZ model with discrete disorder, for which the behavior of number and configurational entropies bear closer similarity with the $U(1)$ LGT, suggesting that the discrete nature of the disorder potential is indeed crucial for understanding the late-time dynamics of entanglement.

MBL-like regime at intermediate coupling

Finally, we address the existence of MBL phase at intermediate couplings $J/w \sim 1$, where a Poisson plateau in the level statistics is clearly seen in Fig. 2. The pertinent question is whether this plateau should be interpreted as the system undergoing an MBL transition in the thermodynamic limit, or if it only arises because the accessible finite-size systems are still impacted by the residual effects of fragmentation at $J/w \to \infty$. Our analysis of entropy jumps in Fig. 6 suggests that the exponent α, although it remains small, steadily rises from zero as J is reduced, suggesting glassy, power-law relaxation dynamics rather than localization. On the other hand, we see $\alpha \to 0$ as N increases, with an increasing saturation time, which is consistent with a logarithmic entanglement growth in the thermodynamic limit. However, at $J \sim w$, DPT is no longer valid and we do not expect to see the jumps in entanglement entropy observed at larger J, hence we do not expect Fig. 6 to accurately capture this regime.

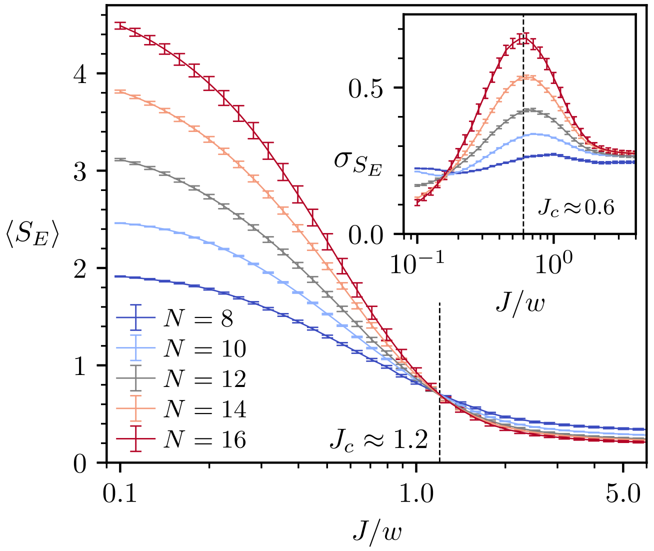

Fig. 7 | Eigenstate entanglement entropy. The mean (main) and standard deviation (inset) of the bipartite entanglement entropy of eigenstates, for 1/3 of eigenstates around the density of states peak in each charge sector. The data is further averaged over all possible sectors for system sizes $N = 8, 10$; 1000 sectors for $N = 12, 14, 16$; and 250 charge sectors for $N = 16$. The dashed black lines mark the "critical" values of the coupling strength J. Error bars indicate the standard uncertainty in the average.

To probe the existence of MBL transition beyond the level statistics, we study the entanglement structure of eigenstates. Close to the middle of the spectrum, the eigenstates of ergodic systems are well-modeled by featureless Haar-random vectors, thus their S_E scales with the volume of the subsystem. By contrast, mid-spectrum eigenstates in the MBL phase can be constructed through quasilocal unitary transformations from product states, hence their S_E follows an area-law[105]. To focus on mid-spectrum properties, we consider 33% of eigenstates around the DOS peak in each charge sector. In disordered spin chain models, a transition from volume-law to area-law entanglement entropy was observed by tuning the disorder strength, accompanied by a diverging variance of S_E at the transition, even within a fixed disorder realization[36]. In finite-size numerics, the crossing point in the mean of S_E of the eigenstates typically provides a lower bound for the critical disorder where the fluctuations of S_E diverge, and the two estimates of the transition do not necessarily coincide in finite-size systems[14].

In Fig. 7, the ergodic nature of the system at small J is witnessed by a volume-law scaling of the mean S_E and the vanishing of its variance. We calculate the mean and standard deviation of S_E for 1/3 of eigenstates around the DOS peak within each charge sector, after which we average the data overcharge sectors. Upon increasing J, we observe the standard deviation peaks at $J_c \approx 0.6$, while the mean entanglement entropies steadily decrease until a crossing occurs at $J_c \approx 1.2$, consistent with an MBL transition. Upon further increasing J, the mean entanglement entropies become approximately independent of system size, as expected for area-law scaling.

Curiously, the variance of S_E in Fig. 7b saturates to a non-zero value at large J. A closer inspection of the distribution of S_E reveals that most eigenstates have either zero or ln 2 entanglement entropy. This can be understood from the Krylov subspaces introduced above. For sufficiently small w/J, the subspaces will not mix, and eigenstates may be decomposed into a product of states within each active region. Let p_{cross} be the proportion of basis states belonging to a Krylov subspace with an active region that crosses the central bond; only that same proportion p_{cross} of eigenstates will have non-zero entanglement entropy for a cut through that bond. If a single

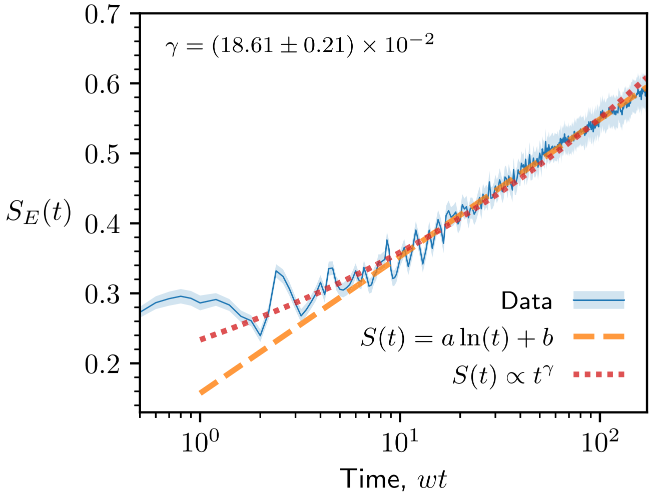

Fig. 8 | Entanglement growth at intermediate coupling strengths. Growth of entanglement entropy from the $|\,\mathrm{vac}\,\rangle$ initial state for system size $N = 50$ at coupling strength $J/w = 3$, obtained via matrix product state simulations (see Methods for details). The data is averaged over 1000 background charge sectors, with the uncertainty in the mean represented by the shading. The dashed lines indicate different types of fits summarized in the legend: a logarithmic fit, and a power-law fit with exponent $\gamma = (6.87 \pm 0.10) \times 10^{-2}$.

particle is delocalized across the boundary, the resultant entanglement entropy will be $\ln 2$, and therefore the mean $\langle S_E \rangle \approx p_{\mathrm{cross}} \ln 2$ and the variance $\sigma_{S_E} \approx \sqrt{p_{\mathrm{cross}}} \ln 2$. We find numerically that, for a random state in the half-filling sector and a random charge sector, the chance that condition (8) is satisfied for the central bond is $\mathcal{O}(N^{-1/2})$ for large N, in accordance with the probability that a random walk has zero displacement[106]. Therefore, we expect $\langle S_E \rangle \propto N^{-1/2}$ and $\sigma_{S_E} \propto N^{-1/4}$, which we observe when we do not restrict to the central one-third of the spectrum but include all eigenstates.

One of the smoking-gun signatures of the MBL phase is the logarithmic in time growth of entanglement entropy from unentangled initial states[92,93], a direct consequence of the the exponentially slow dephasing between LIOMs[94]. In disordered MBL models, this logarithmic growth of entanglement entropy typically persists over many decades in time, e.g., up to times as large as 10^{10} units in the system's natural inverse energy scale[94]. Although in a finite system the entropy eventually saturates, the saturation time increases with system size, hence in the thermodynamic limit, the entropy growth is believed to be unbounded[93].

Entanglement entropy growth for the $U(1)$ LGT model at $J/w = 3$ is presented in Fig. 8. In small systems that can be studied by exact diagonalization, we find the universal regime of entropy growth to be quite short and impacted by the broad approach to the saturation value. Hence, in Fig. 8, we used matrix product state (MPS) simulations in a large system of $N = 50$ spins, as described in the Methods. This allows us to avoid the finite-size effects due to small chain sizes, however the times that can be reached are limited due to the increase in computational effort that comes from the build-up of entanglement. Within the available time range, entropy appears to follow $S_E \sim \ln(t)$ dependence, consistent with MBL. However, the accessible timescales are insufficient to reliably discriminate from power-law dependence, $S_E \sim t^{\gamma}$ (with $\gamma > 0$), as shown by the different fits in Fig. 8. Thus, our data cannot rule out the possibility of slow, power-law delocalization at intermediate J/w values.

Discussion

We have performed a detailed characterization of ergodicity breaking in the lattice Schwinger model as a function of the coupling strength J/w. Standard metrics of quantum chaos, including the level statistics and eigenstate entanglement, with further results on the spectral form factor and many-body Thouless parameter in Supplementary Notes 6, 7, all undergo a sharp change around $J/w \sim 1$. While these results are reminiscent of an emergent MBL phase, as also found in the bosonic lattice Schwinger model[62], we have argued that the observed MBL-like signatures can be accounted for by the residual effects of Hilbert space fragmentation in the infinite-coupling limit. The fragmentation naturally follows from the discretized nature of the model and should be present even in the original fermionic formulation, i.e., prior to substituting dynamical fields for static background charges. Therefore, there are two limits of the model: if we take $J/w \to \infty$, the model remains fragmented even as $N \to \infty$. However, if we take $N \to \infty$ first, at any finite J/w the towers at different energies will mix, and our evidence in Figs. 2 and 6 suggests this will approach Poisson level statistics and an MBL-like regime, although we cannot rule out eventual delocalization.

Furthermore, we have identified the origin of the putative double-logarithmic entanglement growth in the strong-coupling regime[56], presenting its alternative interpretation as a slow approach to the steady state in finite-size systems. Importantly, this entropy growth was shown to occur largely via the rearrangement of particles in subsystems (the configurational entropy), rather than fluctuations in their numbers (the number entropy), as seen in disordered MBL models. We have also identified sharp jumps in the configurational entropy, driven by the resolution of energy scales corresponding to orders of degenerate perturbation theory on the approximately fragmented Hilbert space; it is only when these are averaged that a smooth growth ensues. Based on the statistics of jump times, we conclude that the available numeric data for the entropy growth, including our largest-scale MPS simulations with $N = 50$ spins, cannot discriminate between a power-law or a single-logarithm time dependence. This underscores the difficulty of identifying sub-logarithmic growth based on purely numerical data. Effective models based on random unitary circuits[107] could further extend the timescales in the numerical simulations or provide analytical insights into the functional form of the entanglement growth. While double-logarithmic growth can arise in quenched-disorder MBL models, either as a subleading correction to entanglement entropy[108] or as a leading-order term in particle number fluctuations in a subsystem[51,103,104,109], these effects appear unrelated to the ultraslow entanglement growth in the lattice Schwinger model.

We note that model (1) has been realized with trapped ions[110–113], while the configurational and number entropies have been experimentally measured in ultracold ^{87}Rb atoms in an optical lattice[27]. Thus, quantum simulation platforms could provide further insights into the relation between ergodicity breaking in disordered MBL and the lattice Schwinger model. In particular, current quantum simulation platforms allow the implementation of the tunable topological θ-term that we use here to realize the deconfined phase, and which is responsible for a host of other exotic phenomena such as dynamical topological phase transitions and Coleman's phase transition[114,115]. By tuning the θ-term, distinct forms of ergodicity-breaking have been realized in $U(1)$ quantum link models[115,116]. It would be interesting to further explore the effect of the θ-term on the relation between Hilbert space fragmentation and the rate of entanglement growth in the Schwinger model. Finally, while we have focused on a $U(1)$ LGT in this work, it would be interesting to explore the dynamical effects of fragmentation in non-Abelian LGTs, where forms of weak ergodicity breaking have recently been identified[117,118].

Methods

The structure of the Hilbert space

After a Jordan-Wigner transformation (see Supplementary Note 2), Gauss' law allows us to sequentially integrate out the gauge fields, leading to a Hamiltonian dependent on the background charge sector. In the spin formulation, for each charge sector $\{q_\alpha\}$, the Hamiltonian breaks into two charge-independent terms and a charge-dependent term, given in Eqs. (4)–(6) of the main text. Formally, this corresponds to an XY spin model with a local Z-field and a long-range ZZ coupling. The latter breaks integrability and makes the interactions spatially-asymmetric, with the right-most spin on the lattice completely decoupled from the interaction. The last term of the Hamiltonian, $\hat{H}_q$ in Eq. (6), explicitly depends on the distribution of background charges $\{q_\alpha\}$. For the special case of all background charges q_α being zero, this term takes the form:

$$\hat{H}_{q_\alpha=0} = \frac{J}{2}\sum_{j=1}^{N}\left(\frac{\theta}{\pi}(N-j) - \left\lceil\frac{N-j}{2}\right\rceil\right)\hat{\sigma}_j^z + \frac{m}{2}\sum_{j=1}^{N}(-1)^j\hat{\sigma}_j^z\,, \tag{13}$$

and therefore represents a form of tilted potential. The non-zero background charges can then be viewed as adding disorder to these local fields.

The spin Hamiltonian in Eq. (3) retains the original symmetries of the LGT. The Coulomb and disorder terms in the Hamiltonian are purely diagonal, whereas the purely off-diagonal term $\hat{H}_\pm$ creates and annihilates electron-positron pairs, thus conserving the total particle number. In the spin language, the Hamiltonian conserves the total magnetization $\sum_{i=1}^{N}\hat{\sigma}_i^z$ corresponding to a $U(1)$ symmetry. This is expected as the original continuum theory, QED in $1+1$D has a $U(1)$ gauge symmetry. We resolve this symmetry by working in the sector with zero magnetization, or equivalently the half-filling sector of fermions, which has a Hilbert space dimension of $\binom{N}{N/2}$. In this sector, the model can have further symmetry corresponding to charge conjugation and spatial reflection[113]. However, because of the presence of background charges in $\hat{H}_q$, this is only a symmetry if the background charges $\{q_\alpha\}$ themselves are symmetric under charge conjugation and reflection. For example, this is a symmetry when all background charges are set to zero. For randomly picked charge distributions, however, this is almost never the case and can be ignored.

As mentioned in the main text, the full state of the system is assumed to be a tensor product of the fermionic vacuum state,

$$|\Psi\rangle_f = |101010\ldots\rangle \equiv |\mathrm{vac}\rangle_f, \tag{14}$$

and the superposition of the electric-field eigenstates:

$$|\Psi\rangle_g = \bigotimes_{n=1}^{N-1}|\bar{L}_n\rangle, \quad |\bar{L}_n\rangle = \frac{|-1\rangle_n + |0\rangle_n + |+1\rangle_n}{\sqrt{3}}, \tag{15}$$

where $\hat{L}_n|a\rangle_n = a|a\rangle_n, a \in \mathbb{Z}$.

The choice of the fermionic initial state dictates the relationship between the gauge fields $\hat{L}_n$ and the background charges q_n through the relation:

$$\hat{L}_n = \hat{L}_{n-1} + q_n + \left[\langle\hat{\sigma}_n^z\rangle_{\Psi_f} + (-1)^n\right]/2. \tag{16}$$

The last term vanishes for the Néel state of fermions in Eq. (14), leading to the relation $q_n = \hat{L}_n - \hat{L}_{n-1}$. Thus, the state of the gauge fields $|\bar{L}_n\rangle$ is fully specified in this case by its background charges, which we denote by $|q_n\rangle$. The full initial state then takes the form

$$|\Psi\rangle_0 = \frac{1}{\sqrt{\mathcal{N}}}\sum_{\{q_n\}}|\mathrm{vac}\rangle_f \otimes |q_n\rangle. \tag{17}$$

Since each charge sector admits a Hamiltonian $\hat{H}_{\{q_n\}}$, the sectors are disconnected and the time evolution of the full wave function is described by the average over all sectors:

$$|\Psi(t)\rangle = \frac{1}{\sqrt{\mathcal{N}}}\sum_{\{q_n\}}e^{-i\hat{H}_{\{q_n\}}t}|\mathrm{vac}\rangle_f \otimes |q_n\rangle. \tag{18}$$

As pointed out in ref. 56, the sum in Eq. (18) then acts as an effective disorder average. We diagonalize each $\hat{H}_{\{q_n\}}$ to obtain the spectrum and perform time evolution in individual charge sectors. Exact diagonalization simulations were performed using QuSpin 0.37[119]. For simplicity and to match previous work, rather than calculating q_n from the fields L_n, we draw q_n directly from $\{-1, 0, +1\}$ with uniform probability; we then impose the condition that $\sum_n q_n = 0$, which corresponds to fixing $\hat{L}_0 = \hat{L}_N$ such that there is no net electric charge in the system. Note that restricting to three values on each site leads to the number of background charge sectors scaling as $\mathcal{O}(3^{N-1})$. In principle, the gauge field eigenvalues are unbounded and we could draw the charges q_n from a broader window. This should have effects similar to increasing the strength of $\hat{H}_q$ alone, increasing the strength of fragmentation. In Supplementary Note 8, we show the effects of scaling $\hat{H}_{ZZ}$ and $\hat{H}_q$ independently. On the other hand, if we reduced J while broadening the range of q, we would approach something closer to the uniform disorder seen in typical models of MBL.

Degenerate perturbation theory

To describe dynamics at intermediate times, we developed a degenerate perturbation theory (DPT) approach following Michailidis et al.[120], applicable in the limit $J/w \to \infty$. In this limit, the diagonal part of the Hamiltonian dominates, and we can expand the effective Hamiltonian within a tower $\mathcal{K}_0$, in orders of w/J:

$$\hat{H}_{\mathrm{eff}} = \hat{H}^{[0]} + \hat{H}^{[1]} + \hat{H}^{[2]} + \ldots \tag{19}$$

We denote evolution under DPT up to nth order as DPT(n). The leading term $\hat{H}^{[0]}$ is simply the diagonal parts of the Hamiltonian, $\hat{H}_{ZZ} + \hat{H}_q$, projected into our tower $\mathcal{K}_0$: by definition, this is a constant. $\hat{H}^{[1]}$ is then the projection of $H_\pm$ into $\mathcal{K}_0$, which gives us the Krylov subspaces. Therefore, DPT(1) is simply the dynamics assuming perfect Hilbert space fragmentation. The higher order terms $\hat{H}^{[2]}$ and $\hat{H}^{[3]}$ then provide diagonal and off-diagonal corrections respectively to $\hat{H}_{\mathrm{eff}}$, with the latter in particular connecting different subspaces within $\mathcal{K}_0$. The derivation of $\hat{H}_{\mathrm{eff}}$ up to $\hat{H}^{[3]}$ in provided in the Supplementary Methods.

We note that the full $\hat{H}_{\mathrm{eff}}$ will generate dynamics equivalent to evolution in the full Hilbert space followed by projection into $\mathcal{K}_0$,

$$\hat{P}_0 e^{-i\hat{H}t}|\Psi\rangle = e^{-i\hat{H}_{\mathrm{eff}}t}\hat{P}_0|\Psi\rangle\,, \tag{20}$$

which we refer to as “infinite-order” DPT, or DPT(∞). While this is much more computationally intensive, it is a useful reference point in helping us understand the dynamics of this system in the large-J regime.

We will now compare DPT for the first three non-trivial orders, $n = 1, 2, 3$, to both DPT(∞) as well as full Hamiltonian evolution ("full ED”). In Fig. 9a, we compute the staggered magnetization,

$$\hat{\mu} = \frac{1}{N}\sum_j(-1)^j\hat{\sigma}_j^z\,, \tag{21}$$

following a quench from $|\,\mathrm{vac}\,\rangle$, for the same 256 charge sectors. In the ergodic phase, we expect $\hat{\mu}(t) \to 0$ as $t \to \infty$, but in the MBL phase this should decay to a finite value. Even DPT(1) shows good agreement with both DPT(∞) and full ED for times up to $wt \approx 10^2$, including capturing oscillations in this value at later times, although it fails to capture the decay of these oscillations. For this, we need to go to higher orders, and DPT(3) successfully describes this decay, agreeing with full ED up to $wt \approx 10^4$. We also see that DPT(∞) agrees well with full ED at all times, showing that the dynamics within a J-tower accurately describe the dynamics within the full Hilbert space for local observables.

In Fig. 9b, we then show a similar comparison for the bipartite entanglement entropy, $S_E(t)$(9). This is a highly non-local observable, with a strong dependence on the fine structure of the quantum state, and should be much more challenging to capture. Additionally, in Fig. 9c, we show the mean of the squared difference between finite-order DPT and DPT(∞) in individual charge sectors, which we take as the error in the method and label $\delta S_E(t)$. We see that each successive order of DPT is able to faithfully capture the entanglement entropy attained by DPT(∞) for a factor of approximately $2J/w$ longer in time, up to about $wt \approx 5000$ for DPT(3). We find that these scalings hold as we vary J/w. However, full ED shows a marked difference

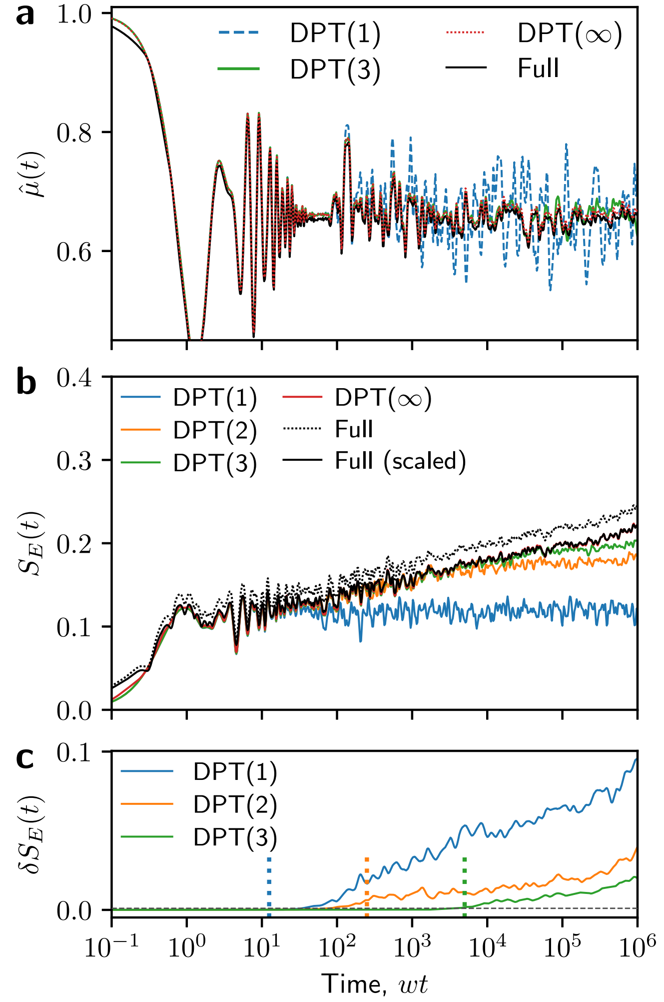

Fig. 9 | Validity of degenerate perturbation theory. a Staggered magnetization $\hat{\mu}(t)$ following a quench from $|\,\mathrm{vac}\,\rangle$, calculated using both 1st- and 3rd-order degenerate pertubation theory (DPT). This is compared to "infinite order" DPT and full Hamiltonian evolution. We exclude 2nd-order DPT to avoid clutter. **b** Bipartite entanglement entropy $S_E(t)$, calculated using the first three orders of DPT, and again compared to DPT(∞) and full exact diagonalization (ED). We also show the full ED rescaled by a constant factor such that it agrees with DPT(∞) at $wt = 10^6$. **c** Error between finite-order DPT and DPT(∞), $\delta S_E(t)$. The vertical dotted lines indicate the rough times beyond which this error grows beyond a small threshold (grey dashed line); these times grow exponentially with the order of DPT. [In all cases, $N = 16$, $J/w = 10$, and we average over the same 256 charge sectors.].

from DPT(∞), showing that dynamics outside the initial J-tower contributes to the entanglement. Despite this, if we rescale the full ED $S_E(t)$ data by a constant factor such that it agrees with DPT(∞) at $wt = 10^6$, then we observe almost perfect agreement between these two methods. This suggests that, while dynamics outside the initial energy level are important, they are both qualitatively and quantitatively similar and do not change the overall functional form, meaning that DPT is able to fully describe the dynamics of the model at short to intermediate times.

We note also that the initial growth in entanglement entropy at $wt < 1$ is captured even in DPT(1). This suggests that it is entirely due to dynamics in active regions that cross the bipartition; because hopping processes elsewhere in the chain do not affect the resonance condition Eq. (8), these distant parts do not interact and so cannot generate entanglement at this order of perturbation theory. Inspecting this more closely, only some charge sectors exhibit this growth, each with an amplitude of ln 2 as would be expected due to the delocalization of a single particle across a partition. The other charge sectors remain at (nearly) zero entanglement, which results in a much smaller spike after averaging over sectors.

Matrix product state simulations

The $U(1)$ LGT Hamiltonian $\hat{H}$ in Eq. (3) can be written as a compact matrix product operator (MPO)[121,122]. Even though $\hat{H}_{ZZ}$ is long-ranged and non-uniform, it couples all sites with a strength that depends solely on the location of the right-hand site. Therefore, $\hat{H}$ can be expressed straightforwardly as an MPO:

$$\hat{H} = \sum_{\{\alpha,\beta\}} \delta_{\alpha_1,0} \left(\prod_{\ell=1}^{N} A^{[\ell]}_{\alpha_\ell,\beta_\ell} \right) \delta_{\beta_N,4}\,, \tag{22}$$

with $A^{[\ell]}$ a rank-4 tensor with entries

$$A^{[\ell]} = \begin{pmatrix} \mathbb{I} & w\hat{\sigma}^{+} & w\hat{\sigma}^{-} & (J/2)\hat{\sigma}^{z} & h_\ell \hat{\sigma}^{z} \\ 0 & 0 & 0 & 0 & \hat{\sigma}^{-} \\ 0 & 0 & 0 & 0 & \hat{\sigma}^{+} \\ 0 & 0 & 0 & \mathbb{I} & (N-\ell)\hat{\sigma}^{z} \\ 0 & 0 & 0 & 0 & \mathbb{I} \end{pmatrix}. \tag{23}$$

We calculate the numerical time evolution of the initial vacuum state using the time-dependent variational principle (TDVP) algorithm[123–125]. We use single-site updates with a dynamically growing bond dimension, fixing the density-matrix truncation threshold. As the MPS bond dimension is continually increasing due to the build-up of entanglement, the computational effort required to perform a single timestep will increase as well, which limits the accessible evolution time for a fixed amount of computation time per charge sector. Furthermore, since each charge sector will have a different entanglement growth rate, the charge sectors with the most rapid growth will limit the largest time for which we can calculate the average over all sectors.

Data availability

The data used to create the figures are available from the corresponding author upon reasonable request. Statement of compliance with EPSRC policy framework on research data: this publication is theoretical work that does not require supporting research data.

Received: 7 October 2024; Accepted: 12 March 2025;

References

1. Wilson, K. G. Confinement of quarks. *Phys. Rev. D.* **10**, 2445–2459 (1974).
2. Kogut, J. & Susskind, L. Hamiltonian formulation of Wilson's lattice gauge theories. *Phys. Rev. D.* **11**, 395–408 (1975).
3. Montvay, I. & Münster, G. *Quantum fields on a lattice* (Cambridge University Press, 1994).
4. Bañuls, M. C. et al. Simulating lattice gauge theories within quantum technologies. *Eur. Phys. J. D.* **74**, 165 (2020).
5. Bauer, C. W. et al. Quantum simulation for high-energy physics. *PRX Quantum* **4**, 027001 (2023).
6. Di Meglio, A. et al. Quantum computing for high-energy physics: State of the art and challenges. *PRX Quantum* **5**, 037001 (2024).
7. Halimeh, J. C., Aidelsburger, M., Grusdt, F., Hauke, P. & Yang, B. Cold-atom quantum simulators of gauge theories. *Nat. Phys.* **21**, 25–36 (2025).
8. Basko, D., Aleiner, I. & Altshuler, B. Metal–insulator transition in a weakly interacting many-electron system with localized single-particle states. *Ann. Phys.* **321**, 1126–1205 (2006).

9. Gornyi, I. V., Mirlin, A. D. & Polyakov, D. G. Interacting electrons in disordered wires: Anderson localization and low-t transport. *Phys. Rev. Lett.* **95**, 206603 (2005).
10. Nandkishore, R. & Huse, D. A. Many-body localization and thermalization in quantum statistical mechanics. *Annu. Rev. Condens. Matter Phys.* **6**, 15–38 (2015).
11. Abanin, D. A., Altman, E., Bloch, I. & Serbyn, M. Colloquium: Many-body localization, thermalization, and entanglement. *Rev. Mod. Phys.* **91**, 021001 (2019).
12. Abanin, D. A. & Papić, Z. Recent progress in many-body localization. *Ann. Phys.* **529**, 1700169 (2017).
13. Alet, F. & Laflorencie, N. Many-body localization: An introduction and selected topics. *C. R. Phys.* **19**, 498–525 (2018).
14. Sierant, P., Lewenstein, M., Scardicchio, A., Vidmar, L. & Zakrzewski, J. Many-body localization in the age of classical computing. *Rep. Prog. Phys.* **88**, 026502 (2025).
15. Sala, P., Rakovszky, T., Verresen, R., Knap, M. & Pollmann, F. Ergodicity breaking arising from Hilbert space fragmentation in dipole-conserving Hamiltonians. *Phys. Rev. X* **10**, 011047 (2020).
16. Khemani, V., Hermele, M. & Nandkishore, R. Localization from Hilbert space shattering: From theory to physical realizations. *Phys. Rev. B* **101**, 174204 (2020).
17. Moudgalya, S., Prem, A., Nandkishore, R., Regnault, N. & Bernevig, B. A. Thermalization and Its Absence within Krylov Subspaces of a Constrained Hamiltonian. In *Memorial Volume for Shoucheng Zhang*, 147–209 (WORLD SCIENTIFIC, Singapore, 2020).
18. Serbyn, M., Abanin, D. A. & Papić, Z. Quantum many-body scars and weak breaking of ergodicity. *Nat. Phys.* **17**, 675–685 (2021).
19. Moudgalya, S., Bernevig, B. A. & Regnault, N. Quantum many-body scars and Hilbert space fragmentation: a review of exact results. *Rep. Prog. Phys.* **85**, 086501 (2022).
20. Chandran, A., Iadecola, T., Khemani, V. & Moessner, R. Quantum many-body scars: A quasiparticle perspective. *Annu. Rev. Condens. Matter Phys.* **14**, 443–469 (2023).
21. Schreiber, M. et al. Observation of many-body localization of interacting fermions in a quasirandom optical lattice. *Science* **349**, 842–845 (2015).
22. yoon Choi, J. et al. Exploring the many-body localization transition in two dimensions. *Science* **352**, 1547–1552 (2016).
23. Bordia, P. et al. Coupling identical one-dimensional many-body localized systems. *Phys. Rev. Lett.* **116**, 140401 (2016).
24. Smith, J. et al. Many-body localization in a quantum simulator with programmable random disorder. *Nat. Phys.* **12**, 907–911 (2016).
25. Roushan, P. et al. Spectroscopic signatures of localization with interacting photons in superconducting qubits. *Science* **358**, 1175–1179 (2017).
26. Rispoli, M. et al. Quantum critical behaviour at the many-body localization transition. *Nature* **573**, 385–389 (2019).
27. Lukin, A. et al. Probing entanglement in a many-body–localized system. *Science* **364**, 256–260 (2019).
28. Léonard, J. et al. Probing the onset of quantum avalanches in a many-body localized system. *Nat. Phys.* **19**, 481–485 (2023).
29. Yao, Y. et al. Observation of many-body fock space dynamics in two dimensions. *Nat. Phys.* **19**, 1459–1465 (2023).
30. Stanley, L. J., Lin, P. V., Jaroszyński, J. & Popović, D. Screening the coulomb interaction leads to a prethermal regime in two-dimensional bad conductors. *Nat. Commun.* **14**, 7004 (2023).
31. Serbyn, M., Papić, Z. & Abanin, D. A. Local Conservation Laws and the Structure of the Many-Body Localized States. *Phys. Rev. Lett.* **111**, 127201 (2013).
32. Huse, D. A., Nandkishore, R. & Oganesyan, V. Phenomenology of fully many-body-localized systems. *Phys. Rev. B* **90**, 174202 (2014).
33. Ros, V., Müller, M. & Scardicchio, A. Integrals of motion in the many-body localized phase. *Nucl. Phys. B* **891**, 420–465 (2015).
34. Imbrie, J. Z. Diagonalization and many-body localization for a disordered quantum spin chain. *Phys. Rev. Lett.* **117**, 027201 (2016).
35. Pal, A. & Huse, D. A. Many-body localization phase transition. *Phys. Rev. B* **82**, 174411 (2010).
36. Kjäll, J. A., Bardarson, J. H. & Pollmann, F. Many-body localization in a disordered quantum ising chain. *Phys. Rev. Lett.* **113**, 107204 (2014).
37. Luitz, D. J., Laflorencie, N. & Alet, F. Many-body localization edge in the random-field Heisenberg chain. *Phys. Rev. B* **91**, 081103 (2015).
38. Bar Lev, Y., Cohen, G. & Reichman, D. R. Absence of diffusion in an interacting system of spinless fermions on a one-dimensional disordered lattice. *Phys. Rev. Lett.* **114**, 100601 (2015).
39. Mondaini, R. & Rigol, M. Many-body localization and thermalization in disordered Hubbard chains. *Phys. Rev. A* **92**, 041601 (2015).
40. Chandran, A., Kim, I. H., Vidal, G. & Abanin, D. A. Constructing local integrals of motion in the many-body localized phase. *Phys. Rev. B* **91**, 085425 (2015).
41. O'Brien, T. E., Abanin, D. A., Vidal, G. & Papić, Z. Explicit construction of local conserved operators in disordered many-body systems. *Phys. Rev. B* **94**, 144208 (2016).
42. Rademaker, L. & Ortuño, M. Explicit local integrals of motion for the many-body localized state. *Phys. Rev. Lett.* **116**, 010404 (2016).
43. Gray, J., Bose, S. & Bayat, A. Many-body localization transition: Schmidt gap, entanglement length, and scaling. *Phys. Rev. B* **97**, 201105 (2018).
44. Mierzejewski, M., Kozarzewski, M. & Prelovšek, P. Counting local integrals of motion in disordered spinless-fermion and Hubbard chains. *Phys. Rev. B* **97**, 064204 (2018).
45. Abanin, D. et al. Distinguishing localization from chaos: Challenges in finite-size systems. *Ann. Phys.* **427**, 168415 (2021).
46. Théveniaut, H., Lan, Z., Meyer, G. & Alet, F. Transition to a many-body localized regime in a two-dimensional disordered quantum dimer model. *Phys. Rev. Res.* **2**, 033154 (2020).
47. Pietracaprina, F. & Alet, F. Probing many-body localization in a disordered quantum dimer model on the honeycomb lattice. *SciPost Phys.* **10**, 044 (2021).
48. Morningstar, A., Colmenarez, L., Khemani, V., Luitz, D. J. & Huse, D. A. Avalanches and many-body resonances in many-body localized systems. *Phys. Rev. B* **105**, 174205 (2022).
49. Jeyaretnam, J., Turner, C. J. & Pal, A. Renormalization view on resonance proliferation between many-body localized phases. *Phys. Rev. B* **108**, 094205 (2023).
50. Panda, R. K., Scardicchio, A., Schulz, M., Taylor, S. R. & Žnidarič, M. Can we study the many-body localisation transition? *Europhys. Lett.* **128**, 67003 (2020).
51. Sierant, P. & Zakrzewski, J. Challenges to observation of many-body localization. *Phys. Rev. B* **105**, 224203 (2022).
52. Šuntajs, J., Bonča, J., Prosen, T. & Vidmar, L. Quantum chaos challenges many-body localization. *Phys. Rev. E* **102**, 062144 (2020).
53. Sels, D. & Polkovnikov, A. Dynamical obstruction to localization in a disordered spin chain. *Phys. Rev. E* **104**, 054105 (2021).
54. Smith, A., Knolle, J., Kovrizhin, D. L. & Moessner, R. Disorder-free localization. *Phys. Rev. Lett.* **118**, 266601 (2017).
55. Smith, A., Knolle, J., Moessner, R. & Kovrizhin, D. L. Absence of ergodicity without quenched disorder: from quantum disentangled liquids to many-body localization. *Phys. Rev. Lett.* **119**, 176601 (2017).
56. Brenes, M., Dalmonte, M., Heyl, M. & Scardicchio, A. Many-body localization dynamics from gauge invariance. *Phys. Rev. Lett.* **120**, 030601 (2018).
57. Metavitsiadis, A., Pidatella, A. & Brenig, W. Thermal transport in a two-dimensional $\mathbb{Z}_2$ spin liquid. *Phys. Rev. B* **96**, 205121 (2017).
58. Nandkishore, R. M. & Sondhi, S. L. Many-body localization with long-range interactions. *Phys. Rev. X* **7**, 041021 (2017).

59. Smith, A., Knolle, J., Moessner, R. & Kovrizhin, D. L. Dynamical localization in $\mathbb{Z}_2$ lattice gauge theories. *Phys. Rev. B* **97**, 245137 (2018).
60. Akhtar, A. A., Nandkishore, R. M. & Sondhi, S. L. Symmetry breaking and localization in a random Schwinger model with commensuration. *Phys. Rev. B* **98**, 115109 (2018).
61. Park, J., Kuno, Y. & Ichinose, I. Glassy dynamics from quark confinement: Atomic quantum simulation of the gauge-higgs model on a lattice. *Phys. Rev. A* **100**, 013629 (2019).
62. Chanda, T., Zakrzewski, J., Lewenstein, M. & Tagliacozzo, L. Confinement and lack of thermalization after quenches in the bosonic Schwinger model. *Phys. Rev. Lett.* **124**, 180602 (2020).
63. Russomanno, A. et al. Homogeneous Floquet time crystal protected by gauge invariance. *Phys. Rev. Res.* **2**, 012003 (2020).
64. Papaefstathiou, I., Smith, A. & Knolle, J. Disorder-free localization in a simple *u*(1) lattice gauge theory. *Phys. Rev. B* **102**, 165132 (2020).
65. McClarty, P. A., Haque, M., Sen, A. & Richter, J. Disorder-free localization and many-body quantum scars from magnetic frustration. *Phys. Rev. B* **102**, 224303 (2020).
66. Hart, O., Gopalakrishnan, S. & Castelnovo, C. Logarithmic entanglement growth from disorder-free localization in the two-leg compass ladder. *Phys. Rev. Lett.* **126**, 227202 (2021).
67. Zhu, G.-Y. & Heyl, M. Subdiffusive dynamics and critical quantum correlations in a disorder-free localized Kitaev honeycomb model out of equilibrium. *Phys. Rev. Res.* **3**, L032069 (2021).
68. Karpov, P., Verdel, R., Huang, Y.-P., Schmitt, M. & Heyl, M. Disorder-free localization in an interacting 2d lattice gauge theory. *Phys. Rev. Lett.* **126**, 130401 (2021).
69. Sous, J., Kloss, B., Kennes, D. M., Reichman, D. R. & Millis, A. J. Phonon-induced disorder in dynamics of optically pumped metals from nonlinear electron-phonon coupling. *Nat. Commun.* **12**, 5803 (2021).
70. Halimeh, J. C. et al. Enhancing disorder-free localization through dynamically emergent local symmetries. *PRX Quantum* **3**, 020345 (2022).
71. Chakraborty, N., Heyl, M., Karpov, P. & Moessner, R. Disorder-free localization transition in a two-dimensional lattice gauge theory. *Phys. Rev. B* **106**, L060308 (2022).
72. Halimeh, J. C., Hauke, P., Knolle, J. & Grusdt, F. Temperature-Induced Disorder-Free Localization https://arxiv.org/abs/2206.11273 (2022).
73. Osborne, J., McCulloch, I. P. & Halimeh, J. C. Disorder-Free Localization in $2+1$D Lattice Gauge Theories with Dynamical Matter https://arxiv.org/abs/2301.07720 (2023).
74. Gao, C. et al. Nonthermal dynamics in a spin-$\frac{1}{2}$ lattice Schwinger model. *Phys. Rev. B* **107**, 104302 (2023).
75. Sala, P., Giudici, G. & Halimeh, J. C. Disorder-free localization as a purely classical effect. *Phys. Rev. B* **109**, L060305 (2024).
76. Hu, Y.-M. & Lian, B. From the quantum breakdown model to the lattice gauge theory. *AAPPS Bull.* **34**, 24–14 (2024).
77. Grover, T. & Fisher, M. P. A. Quantum disentangled liquids. *J. Stat. Mech.: Theory Exp.* **2014**, P10010 (2014).
78. Andraschko, F., Enss, T. & Sirker, J. Purification and many-body localization in cold atomic gases. *Phys. Rev. Lett.* **113**, 217201 (2014).
79. Veness, T., Essler, F. H. L. & Fisher, M. P. A. Quantum disentangled liquid in the half-filled Hubbard model. *Phys. Rev. B* **96**, 195153 (2017).
80. Garrison, J. R., Mishmash, R. V. & Fisher, M. P. A. Partial breakdown of quantum thermalization in a Hubbard-like model. *Phys. Rev. B* **95**, 054204 (2017).
81. Yao, N. Y., Laumann, C. R., Cirac, J. I., Lukin, M. D. & Moore, J. E. Quasi-many-body localization in translation-invariant systems. *Phys. Rev. Lett.* **117**, 240601 (2016).
82. Schiulaz, M., Silva, A. & Müller, M. Dynamics in many-body localized quantum systems without disorder. *Phys. Rev. B* **91**, 184202 (2015).
83. Papić, Z., Stoudenmire, E. M. & Abanin, D. A. Many-body localization in disorder-free systems: The importance of finite-size constraints. *Ann. Phys.* **362**, 714–725 (2015).
84. van Horssen, M., Levi, E. & Garrahan, J. P. Dynamics of many-body localization in a translation-invariant quantum glass model. *Phys. Rev. B* **92**, 100305 (2015).
85. Hickey, J. M., Genway, S. & Garrahan, J. P. Signatures of many-body localisation in a system without disorder and the relation to a glass transition. *J. Stat. Mech.: Theory Exp.* **2016**, 054047 (2016).
86. Enss, T., Andraschko, F. & Sirker, J. Many-body localization in infinite chains. *Phys. Rev. B* **95**, 045121 (2017).
87. van Nieuwenburg, E., Baum, Y. & Refael, G. From Bloch oscillations to many-body localization in clean interacting systems. *PNAS* **116**, 9269–9274 (2019).
88. Schulz, M., Hooley, C. A., Moessner, R. & Pollmann, F. Stark many-body localization. *Phys. Rev. Lett.* **122**, 040606 (2019).
89. Taylor, S. R., Schulz, M., Pollmann, F. & Moessner, R. Experimental probes of stark many-body localization. *Phys. Rev. B* **102**, 054206 (2020).
90. Kloss, B., Halimeh, J. C., Lazarides, A. & Bar Lev, Y. Absence of localization in interacting spin chains with a discrete symmetry. *Nat. Commun.* **14**, 3778 (2023).
91. Chen, J., Chen, C. & Wang, X. Energy- & Symmetry-resolved entanglement dynamics in disordered Bose-Hubbard Chain. https://arxiv.org/abs/2303.14825 (2023).
92. Žnidarič, M., Prosen, Tcv & Prelovšek, P. Many-body localization in the Heisenberg *xxz* magnet in a random field. *Phys. Rev. B* **77**, 064426 (2008).
93. Bardarson, J. H., Pollmann, F. & Moore, J. E. Unbounded growth of entanglement in models of many-body localization. *Phys. Rev. Lett.* **109**, 017202 (2012).
94. Serbyn, M., Papić, Z. & Abanin, D. A. Universal Slow Growth of Entanglement in Interacting Strongly Disordered Systems. *Phys. Rev. Lett.* **110**, 260601 (2013).
95. Mallick, A. & Zakrzewski, J. Anomalous localization in spin chains with tilted interactions. *Phys. Rev. B* **109**, 214206 (2024).
96. Schwinger, J. Quantum electrodynamics. i. a covariant formulation. *Phys. Rev.* **74**, 1439–1461 (1948).
97. Giudici, G., Surace, F. M., Ebot, J. E., Scardicchio, A. & Dalmonte, M. Breakdown of ergodicity in disordered *U*(1) lattice gauge theories. *Phys. Rev. Res.* **2**, 032034 (2020).
98. Oganesyan, V. & Huse, D. A. Localization of interacting fermions at high temperature. *Phys. Rev. B* **75**, 155111 (2007).
99. Mehta, M. L. *Random matrices*, vol. 142 (Elsevier, 2004).
100. Hernandez, V., Roman, J. E. & Vidal, V. Slepc: A scalable and flexible toolkit for the solution of eigenvalue problems. *ACM Trans. Math. Softw.* **31**, 351–362 (2005).
101. Sutherland, B.*Beautiful models: 70 years of exactly solved quantum many-body problems* (World Scientific Publishing Company, 2004).
102. Kim, H. & Huse, D. A. Ballistic spreading of entanglement in a diffusive nonintegrable system. *Phys. Rev. Lett.* **111**, 127205 (2013).
103. Kiefer-Emmanouilidis, M., Unanyan, R., Fleischhauer, M. & Sirker, J. Slow delocalization of particles in many-body localized phases. *Phys. Rev. B* **103**, 024203 (2021).
104. Ghosh, R. & Žnidarič, M. Resonance-induced growth of number entropy in strongly disordered systems. *Phys. Rev. B* **105**, 144203 (2022).
105. Bauer, B. & Nayak, C. Area laws in a many-body localized state and its implications for topological order. *J. Stat. Mech.: Theory Exp.* **2013**, P09005 (2013).

106. Weisstein, E. W. Random walk–1-dimensional. https://mathworld.wolfram.com/RandomWalk1-Dimensional.html. from *MathWorld*—A Wolfram Web Resource. Visited on 08/08/2024.
107. Han, Y., Chen, X. & Lake, E. Exponentially slow thermalization and the robustness of hilbert space fragmentation. https://arxiv.org/abs/2401.11294 (2024).
108. Žnidarič, M. Entanglement in a dephasing model and many-body localization. *Phys. Rev. B* **97**, 214202 (2018).
109. Aceituno Chávez, D., Artiaco, C., Klein Kvorning, T., Herviou, L. & Bardarson, J. H. Ultraslow growth of number entropy in an ℓ-bit model of many-body localization. *Phys. Rev. Lett.* **133**, 126502 (2024).
110. Martinez, E. A. et al. Real-time dynamics of lattice gauge theories with a few-qubit quantum computer. *Nature* **534**, 516–519 (2016).
111. Muschik, C. et al. U(1) Wilson lattice gauge theories in digital quantum simulators. *N. J. Phys.* **19**, 103020 (2017).
112. Kasper, V., Hebenstreit, F., Jendrzejewski, F., Oberthaler, M. K. & Berges, J. Implementing quantum electrodynamics with ultracold atomic systems. *N. J. Phys.* **19**, 023030 (2017).
113. Kokail, C. et al. Self-verifying variational quantum simulation of lattice models. *Nature* **569**, 355–360 (2019).
114. Halimeh, J. C., McCulloch, I. P., Yang, B. & Hauke, P. Tuning the topological θ-angle in cold-atom quantum simulators of gauge theories. *PRX Quantum* **3**, 040316 (2022).
115. Surace, F. M. et al. Lattice gauge theories and string dynamics in Rydberg atom quantum simulators. *Phys. Rev. X* **10**, 021041 (2020).
116. Desaules, J.-Y. et al. Ergodicity Breaking Under Confinement in Cold-Atom Quantum Simulators. *Quantum* **8**, 1274 (2024).
117. Ebner, L., Schäfer, A., Seidl, C., Müller, B. & Yao, X. Entanglement entropy of $2+1$-dimensional SU(2) lattice gauge theory on plaquette chains. *Phys. Rev. D* **110**, https://doi.org/10.1103/PhysRevD.110.014505 (2024).
118. Calajò, G. et al. Quantum Many-Body Scarring in a Non-Abelian Lattice Gauge Theory. https://arxiv.org/abs/2405.13112 (2024).
119. Weinberg, P. & Bukov, M. QuSpin: a Python package for dynamics and exact diagonalisation of quantum many body systems part I: spin chains. *SciPost Phys.* **2**, 003 (2017).
120. Michailidis, A. A. et al. Slow dynamics in translation-invariant quantum lattice models. *Phys. Rev. B* **97**, 104307 (2018).
121. Schollwöck, U. The density-matrix renormalization group in the age of matrix product states. *Ann. Phys.* **326**, 96–192 (2011).
122. Cirac, J. I., Pérez-García, D., Schuch, N. & Verstraete, F. Matrix product states and projected entangled pair states: Concepts, symmetries, theorems. *Rev. Mod. Phys.* **93**, 045003 (2021).
123. Haegeman, J., Lubich, C., Oseledets, I., Vandereycken, B. & Verstraete, F. Unifying time evolution and optimization with matrix product states. *Phys. Rev. B* **94**, 165116 (2016).
124. Paeckel, S. et al. Time-evolution methods for matrix-product states. *Ann. Phys.* **411**, 167998 (2019).
125. McCulloch, I. P. & Osborne, J. J. Matrix product toolkit. https://github.com/mptoolkit.

Acknowledgements

We would like to thank Andrew Hallam and Jean-Yves Desaules for collaboration during the early stages of this project and for useful comments on the manuscript. We acknowledge support by the Leverhulme Trust Research Leadership Award RL-2019-015 and EPSRC grant EP/W026848/1. This research was supported in part by grant NSF PHY-2309135 to the Kavli Institute for Theoretical Physics (KITP). J.C.H. acknowledges support from the Max Planck Society, the Deutsche Forschungsgemeinschaft (DFG, German Research Foundation) under Germany's Excellence Strategy – EXC-2111 – 390814868, and the European Research Council (ERC) under the European Union's Horizon Europe research and innovation program (Grant Agreement No. 101165667)—ERC Starting Grant QuSiGauge. Computational portions of this research work were carried out on ARC3 and ARC4, part of the High-Performance Computing facilities at the University of Leeds, UK. Matrix product state simulations were performed on The University of Queensland's School of Mathematics and Physics Core Computing Facility `getafix`.

Author contributions

All authors contributed to the development of the ideas and analysis of the results. J.J. and T.B. performed exact diagonalization calculations and designed the figures. The MPS simulations were performed by J.J.O. and J.C.H. J.J., T.B., and Z.P. wrote the manuscript with input from other authors.

Competing interests

J.C.H. is a guest editor of the focus "Quantum simulation of gauge theories: steps and strides" for Communications Physics, but was not involved in the editorial review of, or the decision to publish this article. All other authors declare no competing interests.

Additional information

Supplementary information The online version contains supplementary material available at https://doi.org/10.1038/s42005-025-02039-8.

Correspondence and requests for materials should be addressed to Jared Jeyaretnam.

Peer review information *Communications Physics* thanks Rahul Nandkishore, Xiao Chen and the other, anonymous, reviewer(s) for their contribution to the peer review of this work.